

Anatomy-Informed Deep Learning and Radiomics for Automated Neurofibroma Segmentation in Whole-Body MRI

Georgii Kolokolnikov, Marie-Lena Schmalhofer, Lennart Well, Said Farschtschi, Victor-Felix Mautner, Inka Ristow, and René Werner

Abstract—Neurofibromatosis Type 1 is a genetic disorder characterized by the development of neurofibromas (NFs), which exhibit significant variability in size, morphology, and anatomical location. Accurate and automated segmentation of these tumors in whole-body magnetic resonance imaging (WB-MRI) is crucial to assess tumor burden and monitor disease progression. In this study, we present and analyze a fully automated pipeline for NF segmentation in fat-suppressed T2-weighted WB-MRI, consisting of three stages: anatomy segmentation, NF segmentation, and tumor candidate classification. In the first stage, we use the MRSegmentator model to generate an anatomy segmentation mask, extended with a high-risk zone for NFs. This mask is concatenated with the input image as anatomical context information for NF segmentation. The second stage employs an ensemble of 3D anisotropic anatomy-informed U-Nets to produce an NF segmentation confidence mask. In the final stage, tumor candidates are extracted from the confidence mask and classified based on radiomic features, distinguishing tumors from non-tumor regions and reducing false positives. We evaluate the proposed pipeline on three test sets representing different conditions: in-domain data (test set 1), varying imaging protocols and field strength (test set 2), and low tumor burden cases (test set 3). Experimental results show a 68% improvement in per-scan Dice Similarity Coefficient (DSC), a 21% increase in per-tumor DSC, and a two-fold improvement in F1 score for tumor detection in high tumor burden cases by integrating anatomy information. The method is integrated into the 3D Slicer platform for practical clinical use, with the code publicly accessible.

Index Terms—Anatomy-informed models, deep learning, image segmentation, medical image analysis, neurofibroma, whole-body MRI.

This work was supported by DFG grant (DFG SPP 2177), project number 515277218 and the Bundesverband Neurofibromatose e.V. (Corresponding author: Georgii Kolokolnikov).

Georgii Kolokolnikov and René Werner are with the Institute for Applied Medical Informatics, the Institute of Computational Neuroscience, and the Center for Biomedical Artificial Intelligence (bAlome), University Medical Center Hamburg-Eppendorf, 20246 Hamburg, Germany (e-mail: g.kolokolnikov@uke.de; r.werner@uke.de).

Marie-Lena Schmalhofer, Lennart Well, and Inka Ristow are with the Department of Diagnostic and Interventional Radiology and Nuclear Medicine, University Medical Center Hamburg-Eppendorf, 20246 Hamburg, Germany (e-mail: m.schmalhofer@uke.de; l.well@uke.de; i.ristow@uke.de).

Said Farschtschi and Victor-Felix Mautner are with the Department of Neurology, University Medical Center Hamburg-Eppendorf, 20246, Hamburg, Germany (e-mail: s.farschtschi@uke.de; v.mautner@uke.de).

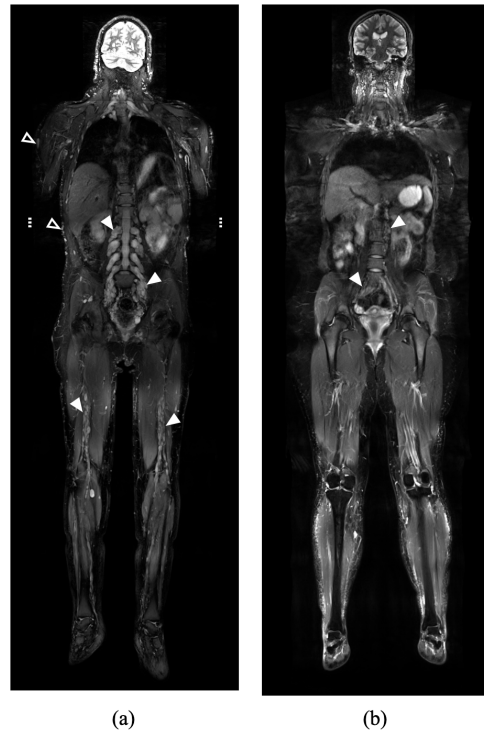


Fig. 1. Fat-suppressed T2-weighted whole-body MRI of two patients with varying tumor burden. (a) 34-year-old male with a tumor burden of 1,591 cm³, showing plexiform neurofibromas (PNFs, filled arrowheads) and subcutaneous neurofibromas (empty arrowheads). (b) 22-year-old female with a tumor burden of 96 cm³, showing PNFs (arrowhead).

I. INTRODUCTION

NEUROFIBROMATOSIS Type 1 (NF1) is an autosomal-dominant genetic disorder affecting 1 in 2,500 to 3,000 individuals [1]. The clinical manifestations of NF1 are diverse, with the hallmark feature being neurofibromas (NFs) distributed throughout the body [2]. NFs (Fig. 1), which can be cutaneous, subcutaneous, or plexiform (PNFs) [3], vary in size, number, and location, leading to disease heterogeneity [4]. Compared to cutaneous and subcutaneous NFs, PNFs are of higher clinical importance due to the elevated risk of transforming into malignant peripheral nerve sheath tumors (MPNSTs). MPNSTs are a leading cause of premature mor-

tality, with a poor five-year survival rate of 21% [5].

Whole-body magnetic resonance imaging (WB-MRI) is an essential tool for assessing tumor burden in NF1 patients [6]. Fat-suppressed T2-weighted (T2w) MR sequences are particularly useful for detecting NFs, as they appear as hyperintense lesions against the surrounding tissue [7].

Traditional approaches to the analysis of WB-MRI of NF1 patients rely on manual tumor volume assessment, which is prone to inter- and intra-observer variability and becomes labor-intensive in high tumor burden cases [4], [8]–[10]. Advances in medical imaging and artificial intelligence have led to the development of promising automated and semi-automated segmentation methods. However, NF segmentation face specific significant challenges:

- **Complex NF morphology.** Variability in NF appearance causes segmentation inconsistencies [9]–[11]. This is, for example, reflected by a reported Dice Similarity Coefficient (DSC) of only 25% for automated nnU-Net-based NF segmentation in 3D WB-MRI [12].
- **Limitations of interactive segmentation techniques.** Semi-automated methods, while reducing manual efforts, remain time-consuming, error-prone, and reliant on user input [10], [12], [13].
- **Scarcity of annotated data.** Only one out of eight [9]–[16] reviewed NF segmentation studies included over 100 WB-MRI scans [12].
- **Lack of standardized evaluation.** Inconsistent evaluation protocols complicate method comparisons [9]–[16].

To address these challenges, we propose and comprehensively validate a novel fully-automated NF segmentation approach. Our key contributions include:

- 1) **Anatomy-informed NF segmentation.** To improve segmentation accuracy, we leverage segmentation masks of organs and add a zone with a high likelihood of NF occurrence (NF high-risk zone) to condition an ensemble of 3D anisotropic U-Nets.
- 2) **Tumor candidate classification.** Focusing on high tumor burden cases, we present a random forest-based classification algorithm that integrates anatomical knowledge and radiomics to correct NF segmentation masks.
- 3) **Pipeline integration into 3D Slicer.** We integrate the proposed segmentation pipeline into 3D Slicer [17], a widely used medical imaging platform, facilitating its use in a clinical environment.

The segmentation pipeline (source code, trained models) is publicly available at <https://github.com/IPMI-ICNS-UKE/NFsegmentationPipeline>. This paper includes a supplementary video demonstrating the proposed NF segmentation pipeline in 3D Slicer. It showcases segmentation and post-processing modes on two fat-suppressed T2w WB-MRI cases. The video is in MP4 format (H.264 codec, 1080p resolution).

II. RELATED WORK

Early work on NF segmentation relied on semi-automated techniques. In 2004, Solomon *et al.* [11] introduced a

thresholding-based method with manual initialization, which was prone to errors in iso-intense regions.

In 2012, Weizman *et al.* [9] proposed a method with manual initialization, followed by a segmentation based on tumor connectivity. It struggled with intensity similarities between PNFs and healthy tissues. A refinement in 2013 utilized a histogram-based tool requiring minimal user input [14]; however, it showed lower accuracy for small-volume tumors and diffusion of segmentation into high-signal-intensity structures adjacent to tumors.

A shift towards deep learning (DL) in NF segmentation was marked by Wu *et al.* in 2020 [15], who introduced the Deep Parametric Active Contour Model (Deep-PAC). It combined active contour models with DL features. Deep-PAC demonstrated superior performance over Fully Convolutional Networks (FCN) and U-Net. However, it required manual initialization and was computationally intensive.

Advancements in fully automated methods were demonstrated by Ho *et al.* in 2020 [13]. They developed a multi-spectral neural network classifier that utilized diffusion-weighted imaging data. Although this method reduced intra- and inter-observer variability, it struggled with misclassifying normal anatomy as pathological.

In 2021, Zhang *et al.* [12] proposed Deep Interactive Networks (DINs), using an Exponential Distance Transform to convert user interactions into guide maps. Compared to 3D U-Net and nnU-Net, DINs achieved significantly higher DSC, though it required user interaction.

In 2022, Wu *et al.* introduced a Deep Hybrid Contextual Feature Network, integrated with a Multi-Gradient Active Contour model [16]. The method consistently outperformed both U-Net and FCN, but it faced challenges due to intensity inhomogeneity and fuzzy boundaries, in addition to numerical instabilities during contour evolution.

Despite progress in NF segmentation, existing methods remain sensitive to tumor appearance variability, are often restricted to 2D operations, or are limited to segmenting only a few tumors within a region of interest. Our approach addresses these limitations by integrating anatomical knowledge and radiomics in a fully automated multistage pipeline.

III. METHODS

This single-center retrospective study was approved by the local ethics committee (2022-300201-WF, 2022-300201_1-WF) with a waiver of informed consent, adhering to data protection regulations and the Declaration of Helsinki.

The proposed novel fully-automated pipeline for NF segmentation in T2w WB-MRI contains three main stages (Fig. 2): anatomy segmentation using the MRSegmentator [18] (Section III-A), NF segmentation using an ensemble of 3D anisotropic anatomy-informed U-Nets (Section III-B), and tumor candidate classification leveraging radiomic features (Section III-C). Since the pipeline does not require user interaction, it reduces the manual workload and potential bias typically present in semi-automated methods [9]–[12], [14], [15]. Furthermore, the pipeline can serve as a pre-segmentation step for refinement by interactive techniques [12], [19], though this is beyond the scope of the current study.

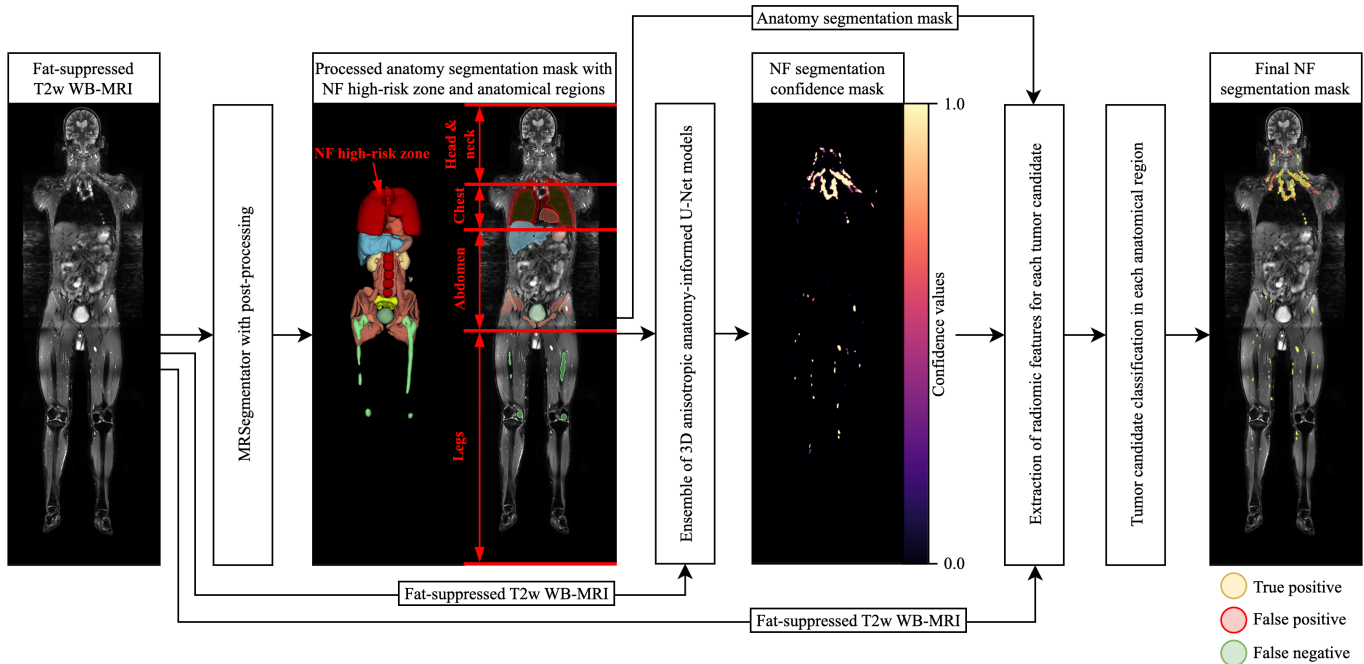


Fig. 2. Proposed pipeline for automated neurofibroma (NF) segmentation, consisting of three main stages: (1) The input T2-weighted whole-body MRI (T2w WB-MRI) is segmented using the MRSegmentator model, followed by post-processing to refine the anatomy segmentation mask. (2) The input T2w WB-MRI and the refined anatomy segmentation mask are processed by an ensemble of 3D anisotropic anatomy-informed U-Net models to produce an NF segmentation confidence mask. (3) The input T2w WB-MRI, the anatomy segmentation mask, and the NF confidence mask are used to extract tumor candidates with their radiomic features. The tumor candidates are grouped by anatomical regions (head and neck, chest, abdomen, legs) and classified using random forest classifiers. The final NF segmentation mask is formed by filtering the tumor candidates.

A. Stage 1: Anatomy Segmentation Using MRSegmentator

1) *Rationale*: NFs are more likely to occur in certain anatomical regions, particularly along the nerves in the head, neck, trunk, and extremities, with a higher concentration around areas such as the spine, brachial plexus, and sciatic nerves [3], [4], [20], [21]. To enhance NF segmentation accuracy, we used anatomical context to focus the neural network model on areas with a higher likelihood of NFs (see Section III-B). This idea is inspired by the prompting strategy in the Segment Anything Model [22]. There, the prompts helped the neural network identify the region of interest.

2) *Prior Anatomical Knowledge*: To extract an anatomy segmentation mask from the input data, we utilized MRSegmentator [18]. Despite its capabilities, the model exhibited limitations when applied to the highly anisotropic fat-suppressed T2w WB-MRIs of this study due to low resolution in certain planes and low contrast of soft tissues. These issues contributed to less reliable segmentation outputs from MRSegmentator as shown in Fig. 3.a, e.g., in structures like the duodenum, small bowel, colon, and bones.

Therefore, the anatomy segmentation was refined by post-processing and incorporating anatomical knowledge of typical NF locations [3], [4], [20], [21]. Organs with DSC below 0.85 on the NAKO dataset [18] and vessels were excluded due to poor segmentation performance. Additionally, paired organs were merged, and muscle groups were consolidated into one label (Table I).

Based on prior knowledge about typical NF localizations

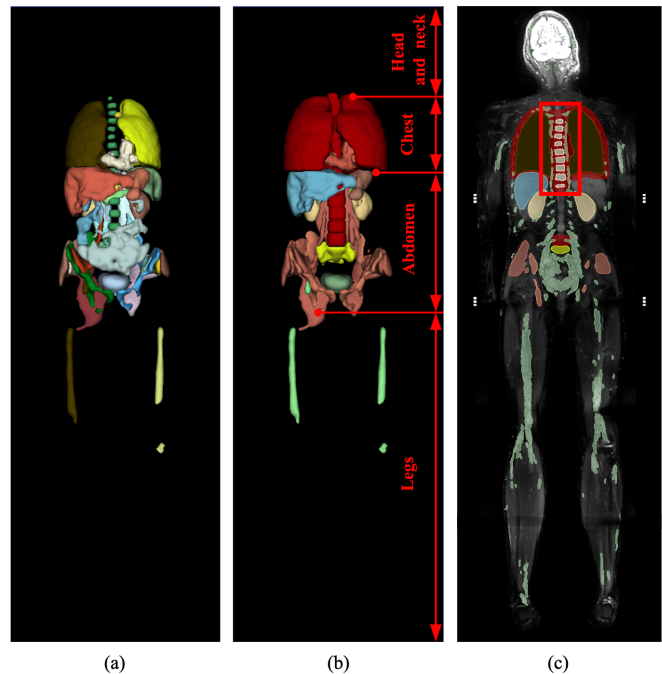


Fig. 3. Comparison of initial and refined anatomy segmentation masks: (a) Initial coarse anatomy segmentation mask generated by MRSegmentator. (b) Refined mask with redundant anatomies removed, labels merged, neurofibroma (NF) high-risk zone added (red structure around the lungs and spine), and anatomical regions (red arrows) defined by anatomical landmarks: the highest and the lowest points of the lungs, and the lowest point of the hips (red dots). (c) T2-weighted whole-body MRI with updated anatomy segmentation masks and NF ground truth (green), highlighting NFs within the NF high-risk zone (red rectangle).

TABLE I
ANATOMY SEGMENTATION MASK CONSTRUCTION BASED ON
REPORTED MRSEGMENTATOR PERFORMANCE AND KNOWLEDGE OF
TYPICAL NEUROFIBROMA (NF) LOCALIZATIONS

Organs	DSC	NF can be inside	NF can be in proximity	Included in the mask
Heart	0.95	No	Yes	Yes
Lungs	0.97	No	Yes	Yes (merged)
Esophagus	0.84	No	Yes	No
Liver	0.95	No	No	Yes
Spleen	0.89	No	No	Yes (merged into stomach)
Pancreas	0.75	No	No	No
Gallbladder	0.74	No	No	No
Stomach	0.89	No	No	Yes
Duodenum	0.76	No	No	No
Small bowel	0.75	No	Yes	No
Colon	0.81	No	Yes	No
Kidneys	0.88 / 0.90	No	Yes	Yes (merged)
Adrenal glands	0.65 / 0.61	No	Yes	No
Urinary bladder	0.95	No	Yes	Yes
Spine	0.89	Yes	Yes	Yes
Sacrum	0.87	Yes	Yes	Yes
Hips	0.89 / 0.89	No	Yes	Yes (merged)
Femurs	0.94 / 0.93	No	Yes	Yes (merged)
Gluteus maximus muscles	0.85 / 0.91	Yes	Yes	Yes (merged into muscles)
Gluteus medius muscles	0.92 / 0.90	Yes	Yes	Yes (merged into muscles)
Gluteus minimus muscles	0.88 / 0.89	Yes	Yes	Yes (merged into muscles)
Autochthonous muscles	0.94 / 0.94	Yes	Yes	Yes (merged into muscles)
Iliopsoas muscles	0.92 / 0.91	Yes	Yes	Yes (merged into muscles)
Aorta	0.90	No	Yes	No
Inferior vena cava	0.81	No	Yes	No
Portal/splenic vein	0.54	No	Yes	No
Iliac arteries	0.77 / 0.72	No	Yes	No
Iliac veins	0.80 / 0.82	No	Yes	No

DSC – reported Dice Similarity Coefficient of MRSegmentator on the NAKO Dataset [18].

[3], [4], [20], [21], we defined an NF high-risk zone near the lungs (around ribs and intercostal nerves) and the spine (near spinal nerves). The NF high-risk zone, i.e. areas with a high probability of the occurrence of NFs, was added as a separate label to the anatomy segmentation mask by dilating segmentation masks of the lungs and spine.

The refined mask (Fig. 3.b) included 11 organ labels and an additional label for the NF high-risk zone. Fig. 3.c shows NFs within the labeled NF high-risk zone. We also defined specific anatomical regions based on landmarks:

- **Head and neck.** Above the highest point of the lungs.
- **Chest.** Between the lungs’ lowest and highest points.

- **Abdomen.** Between the lowest point of the lungs and the lowest point of the hips (ischium).
- **Legs.** Below the lowest point of the hips.

B. Stage 2: Neurofibroma Segmentation Using an Ensemble of 3D Anisotropic Anatomy-Informed U-Nets

1) *Anisotropy of NF Data:* The T2w WB-MRI data are highly anisotropic, with the anterior-posterior axis voxel size being over ten times larger than for the cranio-caudal and lateral axes. We hypothesized that maintaining this anisotropic spacing during processing can improve segmentation accuracy by avoiding interpolation artifacts. We, therefore, resampled the data to a unified mean anisotropic spacing derived from the dataset for consistency (see Section IV-A.2).

2) *Segmentation Model Architecture:* We selected U-Net as the backbone architecture for its versatility. Unlike data-hungry transformer-based models (e.g., UNETR, Swin UNETR) [23], [24], U-Net is more suitable for datasets with limited samples, like in the NF segmentation case.

Our approach differs from previous methods [9]–[13], [15], [16] by leveraging anatomical context to enhance NF segmentation accuracy. We concatenated the anatomy segmentation mask with the T2w WB-MRI as a two-channel input to guide the neural network to focus on specific regions within the T2w WB-MRI. While multiple methods exist to integrate anatomical knowledge into neural networks [12], [19], [22], [25], we opted for this simpler concatenation method to minimize architectural changes to the baseline U-Net model. This allowed us to more directly assess the impact of anatomical knowledge on segmentation performance.

To handle anisotropy, the 3D anisotropic U-Net maintained the original voxel resolution. With a patch size of 10 x 640 x 256, it balanced computational efficiency and anatomical context. The nnU-Net framework [26] was applied to optimize the architecture, featuring seven encoder and six decoder stages with convolutional blocks, instance normalization, and leaky rectified linear unit activation. Strides and kernel sizes were adapted to downsample along cranio-caudal and lateral axes while preserving anterior-posterior resolution. A 1x1x1 convolution with sigmoid activation mapped tumor probability.

3) *Ensembling:* We employed an ensemble of three 3D anisotropic anatomy-informed U-Nets, each trained with random initialization and different data splits via three-fold cross-validation. The tumor probability masks of the individual models were averaged to reduce variance and bias in predictions, generating an NF segmentation confidence mask.

C. Stage 3: Tumor Candidate Classification

1) *Rationale:* The tumor candidate classification step was introduced to improve specificity in NF segmentation, i.e., the reduction the number of typical misclassification of non-tumorous tissues like muscles and fat as NFs.

2) *Extracting Tumor Candidates:* After generating the NF segmentation confidence mask, thresholding was applied to distinguish tumors from the background. The confidence threshold, a hyperparameter, balanced true tumor detection against false positives. A higher confidence threshold (0.5 -

default value) minimized false positives but could miss some true tumors (false negatives), whereas a lower confidence threshold (0.25 - median of the lowest confidence values in the predicted NF segmentation masks) captured more true tumors but increased false positives. Based on the resulting binary mask, component analysis was used to identify tumor candidates, grouped by anatomical region to account for appearance variability.

3) *Extracting Radiomic Features*: For each tumor candidate, we extracted 800 radiomic features (shape, intensity, texture) using PyRadiomics [27], leveraging their potential for NF tumor classification [28], [29]. Feature selection followed standard radiomics workflow [30]: removal of features with near-zero variance, retention of non-intercorrelated features using Spearman correlation, and selection of the top 10 features via recursive feature elimination with a random forest classifier.

4) *Classification*: Selected features describing each tumor candidate were classified using region-specific random forest classifiers to account for NF variability across anatomical regions. Random forests were chosen as classifiers for their robustness and ability to handle small datasets and high-dimensional feature spaces [31]. Identified non-tumor candidates were excluded, forming the final NF segmentation mask.

IV. EXPERIMENTS

A. Data Description

1) *Source of Data*: The NF dataset was acquired at the neurofibromatosis outpatient clinic at the University Medical Center Hamburg-Eppendorf, using a Siemens Magnetom scanner (Siemens Healthineers, Erlangen, Germany). The inclusion criteria were: confirmed NF1 diagnosis [32], no ongoing medication, and availability of WB-MRIs with documented peripheral nerve sheath tumors. T2w WB-MRIs were collected over 14 years (2006–2020), and tumor segmentation was manually performed by two radiologists (I.R. and M.-L. S.).

2) *Demographic, Imaging, and Clinical Characteristics*: The NF dataset included 109 T2w WB-MRI scans from 74 patients (37 males, 37 females; mean age: 29.7 years). The scans had high anisotropy (in-plane resolution of 0.63 mm x 0.63 mm; mean slice thickness of 7.79 mm). Ground truth annotations focused on PNFs due to their elevated risk of malignant transformation. A summary of the demographic and imaging characteristics of the data is presented in Table II.

Tumor burden and count varied across the patients with differences in anatomical distribution (Fig. 4). The abdomen and legs were the most affected regions, displaying the highest tumor volumes and counts, whereas the chest, head, and neck were less involved, consistent with previous findings [4].

3) *Dataset Partitioning*: To evaluate the NF segmentation performance in different scenarios, the NF dataset was split into a train and three distinct test sets. The partitioning strategy was as follows: patients scanned with a 1.5T MRI were allocated to Test Set #2 (out-of-domain). For the remaining 3T scans, the tumor burden distribution was analyzed, and cases in the first quartile (tumor burden <47 cm³) were assigned to Test Set #3 (low tumor burden). The remaining cases were randomly split between the train and Test Set #1 (in-domain) at the patient level. A summary of each set is provided below:

TABLE II
DEMOGRAPHIC AND IMAGING CHARACTERISTICS OF THE NEUROFIBROMA DATASET

Parameter	Value
T2w WB-MRI scans, total (n)	109
Train set	63
Test set #1	13
Test set #2	11
Test set #3	22
Patients, total (n)	74
Train set	42
Test set #1	13
Test set #2	9
Test set #3	10
Sex, total (m / f)	37 / 37
Train set	21 / 21
Test set #1	8 / 5
Test set #2	3 / 6
Test set #3	5 / 5
Mean age at scanning, total (years, mean \pm SD)	29.7 \pm 14.3
Train set	31.9 \pm 13.4
Test set #1	32.5 \pm 13.6
Test set #2	27.7 \pm 13.6
Test set #3	22.4 \pm 15.7
Imaging characteristics	3T and 1.5T, 8 different MRI protocols
Train set	3T, 3 different MRI protocols
Test set #1	3T, 2 different MRI protocols
Test set #2	1.5T, 5 different MRI protocols
Test set #3	3T, 2 different MRI protocols

T2w WB-MRI – T2-weighted whole-body MRI, SD – standard deviation, m – male, f – female.

- **Train set**. Showed a wide range of tumor burdens (median: 618.2 cm³; interquartile range (IQR): 1276.9 cm³) and counts (median: 224 tumors per scan; IQR: 319). The abdomen had the highest tumor burden (median volume: 219.9 cm³; IQR: 690.8 cm³; median count: 72.2), and the legs had the highest tumor count (median volume: 115.2 cm³; IQR: 306.7 cm³; median count: 99.5).
- **Test set #1 (in-domain)**. Included scans that matched the train set in terms of MRI protocols, field strength, and tumor burden to assess the model performance under known conditions. This set had the highest tumor burden (median: 1311.2 cm³; IQR: 3872.1 cm³) and showed significant variability in tumor counts (median: 62; IQR: 608). Tumor burden and variability were high across all regions, especially in the legs (median volume: 490.8 cm³; IQR: 921.9 cm³; median count: 120.5).
- **Test set #2 (out-of-domain)**. Included scans acquired with different MRI protocols (repetition time, echo time, flip angle) and at a lower field strength (1.5T compared to 3T used in the train set) to assess the model generalization ability across varying imaging environments. This set demonstrated moderate tumor burden (median: 442.4 cm³; IQR: 512.1 cm³) and count (median: 112; IQR: 288), with the abdomen (median volume: 139.3 cm³; IQR: 145.9 cm³; median count: 58.9) and legs (median volume: 97.4 cm³; IQR: 227.9 cm³; median count: 79.9) being the most affected regions.
- **Test set #3 (low tumor burden)**. Included scans from patients with low tumor burden (median: 5.6 cm³; IQR:

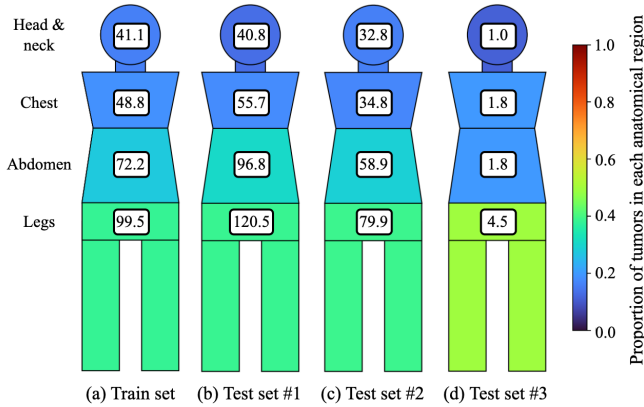


Fig. 4. Distribution of tumors across anatomical regions in four datasets: (a) Train set; (b) Test set #1; (c) Test set #2; (d) Test set #3. Each dataset is represented by a stylized human figure divided into anatomical regions. The numerical values within each region indicate the average absolute number of tumors in that region. The color of each region represents the proportion of tumors in that region relative to the total tumor count in each dataset, as indicated by the color bar.

10.9 cm³) and count (median: 2; IQR: 5), allowing assessment of model sensitivity to sparse tumors. Tumor burden was minimal across anatomical regions.

B. Experimental Design

The segmentation performance of the proposed pipeline was evaluated for the described three test sets. First, we compared a baseline 3D isotropic U-Net (input patch size: 128 x 128 x 128; spacing: 1.0 mm x 1.0 mm x 1.0 mm) with the 3D anisotropic U-Net (input patch size: 10 x 640 x 256; spacing: 7.8 mm x 0.625 mm x 0.625 mm) to assess the impact of anisotropic image processing. Next, we evaluated the benefit of anatomical knowledge integration by comparing the 3D anisotropic U-Net with a 3D anisotropic anatomy-informed U-Net that used two-channel input (T2w WB-MRI and anatomy segmentation mask). Finally, we tested the effect of tumor candidate classification by comparing an ensemble of 3D anisotropic anatomy-informed U-Nets with and without this post-processing step, employing both low- and high-confidence thresholds.

C. Evaluation Metrics

We used several metrics to evaluate NF segmentation performance, including DSC, Volume Overlap Error (VOE), and Absolute Relative Volume Difference (ARVD). DSC, a widely used metric for assessing spatial overlap [26], was calculated per scan and per tumor. VOE and ARVD, which quantify volumetric differences, were included for consistent comparison with the previous study [12].

While DSC, VOE, and ARVD measured the accuracy of tumor segmentation, the F1 score was used to assess the NF detection performance per scan and anatomical region. This metric required calculating True Positives (TP), False Positives (FP), and False Negatives (FN). A tumor instance from a ground truth mask was counted as a TP if it overlapped with a

prediction, and as an FN if it did not. A tumor instance from a predicted segmentation mask was counted as an FP if it did not match any ground truth.

D. Implementation Details

The NF segmentation pipeline was implemented in Python 3.9 and integrated into 3D Slicer [17] via MONAI Label. U-Net models were built using MONAI [33] and PyTorch, with architecture refinement via the nnU-Net framework. Image processing used SimpleITK, and anatomy segmentation relied on the MRSegmentator repository. Tumor candidate classification utilized PyRadiomics for feature extraction, Scikit-Learn for feature selection and random forest-based classification. All experiments were run on two NVIDIA RTX A6000 GPUs.

The 3D anisotropic anatomy-informed U-Net model had a batch size of 2 with 2-channel inputs (T2w WB-MRI and anatomy segmentation mask). We applied Z-score normalization to T2w WB-MRI images to standardize the intensity distribution across different scans, compensating for variability in MRI protocols and acquisition parameters. The anatomy segmentation masks were rescaled to the range 0-1, maintaining numerical stability during training. The model was trained with generalized Dice Focal Loss for imbalanced segmentation, and optimized with the AdamW algorithm (weight decay = 5×10^{-5}). An initial learning rate of 1×10^{-4} was decayed by 0.99 per epoch over 1000 epochs, with the best validation checkpoint used as the final model. We used 3-fold cross-validation. Inference was performed using a sliding window approach with a 25% overlap.

V. RESULTS

A. Neurofibroma Segmentation Performance

We evaluated six NF segmentation methods across three test sets to determine improvements over the baseline (Table III): a baseline 3D isotropic U-Net, a 3D anisotropic U-Net, a 3D anisotropic anatomy-informed U-Net, an ensemble of 3D anisotropic anatomy-informed U-Nets, and ensembles of 3D anisotropic anatomy-informed U-Nets with low- and high-confidence tumor candidate classification. The low-confidence threshold used for tumor candidate classification was set at the median of the lowest confidence values in the predicted NF segmentation masks, and the high-confidence threshold at a default value of 0.5.

First, the segmentation metrics were calculated per scan. Methods incorporating anisotropy handling and anatomical knowledge outperformed the baseline across all test sets. Ensembling-based method further improved performance in datasets with higher variability in MRI protocols and tumor presentation (Test set #2 and #3). Tumor candidate classification had mixed results. The ensemble of the 3D anisotropic anatomy-informed U-Nets with low-confidence tumor candidate classification achieved the highest per-scan DSC of 0.64 on Test set #1, representing a 68.4% increase over the baseline. For Test set #2 and #3, the ensembling-based methods without and with high-confidence tumor candidate classification achieved the highest per-scan DSCs of 0.51 and 0.23, respectively.

TABLE III

SEGMENTATION PERFORMANCE OF SIX METHODS ACROSS THREE TEST SETS. METHODS: (1) 3D ISOTROPIC U-NET, (2) 3D ANISOTROPIC U-NET, (3) 3D ANISOTROPIC ANATOMY-INFORMED U-NET, (4) ENSEMBLE OF 3D ANISOTROPIC ANATOMY-INFORMED U-NETS, (5, 6) ENSEMBLE OF 3D ANISOTROPIC ANATOMY-INFORMED U-NETS WITH LOW AND HIGH-CONFIDENCE TUMOR CANDIDATE CLASSIFICATION, RESPECTIVELY.

Method i	1	2	3	4	5	6
Test set #1						
Per-scan DSC (Mean \pm SD) \uparrow	0.38 \pm 0.23	0.54 \pm 0.23	0.60 \pm 0.17	0.62 \pm 0.16	0.64 \pm 0.13	0.63 \pm 0.15
p -value (Method i vs $i - 1$)	-	< 0.01	< 0.01	0.09	0.87	0.62
Per-tumor DSC (Mean \pm SD) \uparrow	0.71 \pm 0.09	0.78 \pm 0.09	0.80 \pm 0.14	0.79 \pm 0.12	0.81 \pm 0.12	0.86 \pm 0.10
p -value (Method i vs $i - 1$)	-	< 0.01	0.23	0.34	0.06	< 0.01
Test set #2						
Per-scan DSC (Mean \pm SD) \uparrow	0.23 \pm 0.15	0.48 \pm 0.16	0.50 \pm 0.12	0.51 \pm 0.14	0.50 \pm 0.13	0.51 \pm 0.15
p -value (Method i vs $i - 1$)	-	< 0.01	0.97	< 0.01	< 0.01	< 0.01
Per-tumor DSC (Mean \pm SD) \uparrow	0.75 \pm 0.22	0.73 \pm 0.20	0.79 \pm 0.12	0.77 \pm 0.20	0.78 \pm 0.22	0.86 \pm 0.11
p -value (Method i vs $i - 1$)	-	0.52	0.02	0.76	0.68	< 0.01
Test set #3						
Per-scan DSC (Mean \pm SD) \uparrow	0.02 \pm 0.01	0.16 \pm 0.18	0.22 \pm 0.23	0.23 \pm 0.24	0.20 \pm 0.22	0.23 \pm 0.24
p -value (Method i vs $i - 1$)	-	< 0.01	< 0.01	< 0.01	< 0.01	< 0.01
Per-tumor DSC (Mean \pm SD) \uparrow	0.85 \pm 0.19	0.83 \pm 0.19	0.85 \pm 0.18	0.81 \pm 0.24	0.88 \pm 0.14	0.89 \pm 0.18
p -value (Method i vs $i - 1$)	-	0.52	0.04	0.05	< 0.01	0.54

DSC – Dice Similarity Coefficient, SD – standard deviation. The highest metric values are in bold. Statistical significance was evaluated using the Wilcoxon signed-rank test for paired per-scan DSC between consecutive methods (Method i vs. Method $i - 1$), with Bonferroni correction for multiple comparisons.

Next, we evaluated per-tumor DSC for correctly detected tumors. Across all test sets, methods with anisotropic configurations, anatomical knowledge, and ensembling strategies consistently performed better than the baseline. However, the highest gains were observed with the ensemble of 3D anisotropic anatomy-informed U-Nets with high-confidence tumor candidate classification. This method achieved per-tumor DSC scores of 0.86, 0.86, and 0.89 on Test sets #1, #2, and #3, showing significant improvements of 21.1%, 14.7%, and 4.7% over the baseline, respectively.

Based on these results, we selected the following methods for further analysis:

- Baseline 3D isotropic U-Net (henceforth denoted as Method 1).
- 3D anisotropic U-Net (denoted as Method 2).
- Ensemble of 3D anisotropic anatomy-informed U-Nets (denoted as Method 3).
- Method 3 with high-confidence tumor candidate classification (denoted as Method 4).

B. Neurofibroma Detection Performance

1) *Per-Scan Analysis*: We compared the tumor detection performance using per-scan F1 scores across three test sets (Table IV). Method 2 (i.e., anisotropic U-Net) significantly outperformed Method 1 (baseline) across all sets. Method 3 (with anatomical knowledge and ensembling) improved the results on Test set #3 but did not consistently outperform Method 2 on the other sets. Method 4 (with tumor candidate classification) achieved the highest F1 scores of 0.44, 0.54, and 0.17 on Test set #1, #2, and #3, corresponding to increases of 110%, 170%, and 1600% over the baseline, although the improvement over Method 3 on Test set #3 was not statistically significant.

2) *Analysis Per Anatomical Region*: We analyzed mean F1 scores for tumor detection across anatomical regions: head and neck, chest, abdomen, and legs (Fig. 5). Performance generally

TABLE IV
PER-SCAN F1 SCORES FOR TUMOR DETECTION PERFORMANCE ACROSS THREE TEST SETS. METHODS: (1) 3D ISOTROPIC U-NET, (2) 3D ANISOTROPIC U-NET, (3) ENSEMBLE OF 3D ANISOTROPIC ANATOMY-INFORMED U-NETS, (4) METHOD 3 WITH HIGH-CONFIDENCE TUMOR CANDIDATE CLASSIFICATION

Method i	1	2	3	4
Test set #1				
Per-scan F1 score (Mean \pm SD) \uparrow	0.21 \pm 0.21	0.40 \pm 0.23	0.40 \pm 0.22	0.44 \pm 0.23
p -value (Method i vs $i - 1$)	-	< 0.01	0.52	0.02
Test set #2				
Per-scan F1 score (Mean \pm SD) \uparrow	0.20 \pm 0.17	0.46 \pm 0.22	0.48 \pm 0.21	0.54 \pm 0.22
p -value (Method i vs $i - 1$)	-	< 0.01	0.97	< 0.01
Test set #3				
Per-scan F1 score (Mean \pm SD) \uparrow	0.01 \pm 0.01	0.14 \pm 0.12	0.17 \pm 0.14	0.17 \pm 0.13
p -value (Method i vs $i - 1$)	-	< 0.01	< 0.01	0.52

SD – standard deviation. The highest metric values are in bold. Statistical significance was evaluated using the Wilcoxon signed-rank test for paired per-scan F1 score between consecutive methods (Method i vs. Method $i - 1$), with Bonferroni correction for multiple comparisons.

improved with method complexity, from Method 1 to Method 4. Methods 2 (anisotropic U-Net) and 3 (with anatomical knowledge and ensembling) showed gradual improvements, whereas Method 4 (with tumor candidate classification) consistently outperformed the others in most regions.

All methods performed best in the legs region, indicating fewer challenges for tumor detection in the lower body. The chest and abdomen regions showed moderate performance. The head and neck was the most challenging region for tumor detection, with the lowest mean F1 scores across all methods.

C. Domain Shift Robustness Analysis

We assessed the robustness of NF segmentation methods to domain shifts by analyzing performance degradation when the

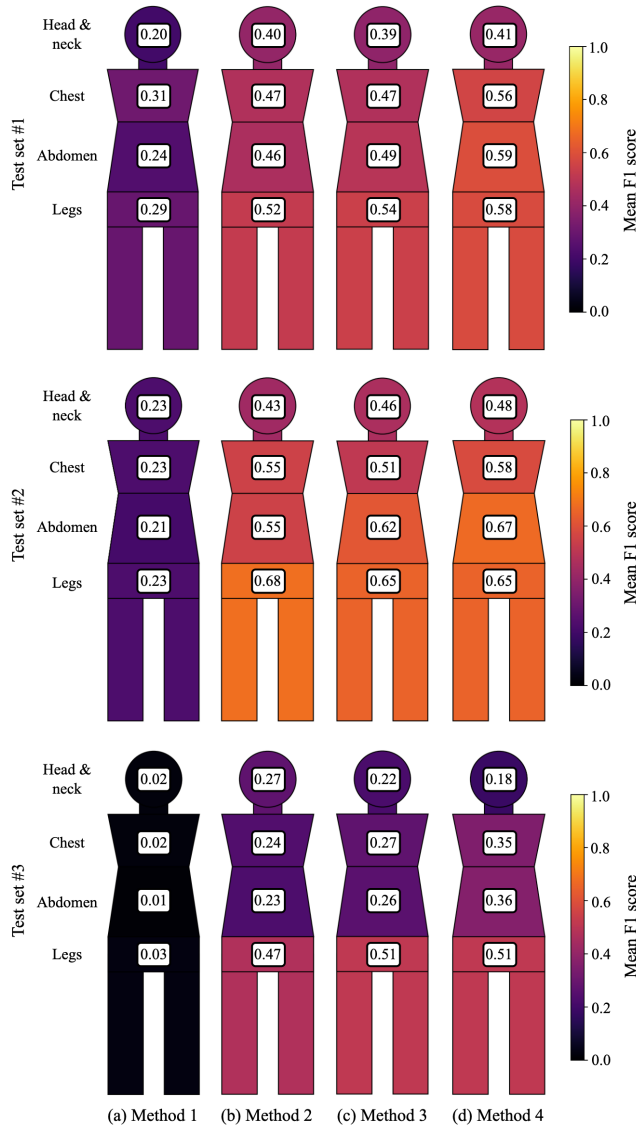


Fig. 5. Mean F1 scores for tumor detection across anatomical regions for three test sets #1, #2, #3 (rows), and four methods (columns): (a) Method 1 (3D isotropic U-Net), (b) Method 2 (3D anisotropic U-Net), (c) Method 3 (ensemble of 3D anisotropic anatomy-informed U-Nets), (d) Method 4 (Method 3 with tumor candidate classification).

neural networks trained on 3T MRI were tested on 1.5T MRI dataset (Test set #2). Performance changes were measured using per-scan DSC (Fig. 6). The analysis revealed varying levels of robustness to domain shifts. Methods 1 (baseline), 2 (with anisotropy), and 3 (with anatomical knowledge and ensembling) experienced moderate performance differences, although these changes were not statistically significant. Method 4 (with tumor candidate classification) exhibited a statistically significant performance drop, indicating limited robustness to changes in MRI field strength compared to other methods.

VI. DISCUSSION

A. Performance Analysis of Neurofibroma Segmentation

1) *Key Findings and Implications*: Introducing anisotropy into the U-Net architecture significantly improved NF seg-

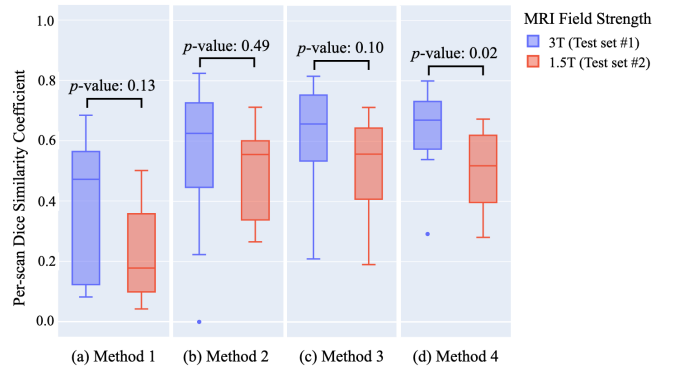


Fig. 6. Degradation in neurofibroma segmentation performance (measured by per-scan Dice Similarity Coefficient) of methods tested on datasets with different MRI field strength (3T in Test set #1 vs. 1.5T in Test set #2), with corresponding p-values: (a) Method 1 (3D isotropic U-Net), (b) Method 2 (3D anisotropic U-Net), (c) Method 3 (ensemble of 3D anisotropic anatomy-informed U-Nets), (d) Method 4 (Method 3 with high-confidence tumor candidate classification).

TABLE V
COMPARISON OF THE ENSEMBLE OF 3D ANISOTROPIC ANATOMY-INFORMED U-NETS WITH TUMOR CANDIDATE CLASSIFICATION (METHOD 4) AGAINST PREVIOUS STUDIES [12]

Method	Dataset	DSC \uparrow	VOE \downarrow	ARVD \downarrow
Auto - DeepMedic	DINs study	0.06	0.97	77.95
Auto - 3D U-Net	DINs study	0.06	0.97	77.62
Auto - nnU-Net	DINs study	0.25	0.84	5.98
Interactive - DINs	DINs study	0.69	0.45	0.64
Method 4	Test set #1	0.63	0.53	0.64
Method 4	Test set #2	0.51	0.64	1.12
Method 4	Test set #3	0.23	0.83	12.69

DSC – Dice Similarity Coefficient, VOE – Volume Overlap Error, ARVD – Absolute Relative Volume Difference.

mentation, with the 3D anisotropic U-Net outperforming the baseline 3D isotropic U-Net, especially for hard-to-segment anatomical regions (e.g., improved segmentation in head, cases 1 and 3, Fig. 7). The 3D anisotropic anatomy-informed U-Net enhanced performance by leveraging anatomical context to focus on likely NF regions, increasing true positive rates (e.g., improved segmentation in superior mediastinum, case 1, Fig. 7). The ensemble strategy with tumor candidate classification achieved the best overall performance, reducing false positives by using radiomic features to distinguish tumors from non-tumor regions. It also improved segmentation in low-confidence areas, capturing larger tumor regions in diffuse NF cases (Fig. 7, cases 2 and 3). However, this method was more sensitive to domain shifts.

2) *Comparison with Previous Studies*: Direct comparison with other studies is limited by data availability, but we benchmarked our findings across diverse datasets against [12], as both used the same evaluation protocol (Table V). Compared to the nnU-Net baseline, our method showed superior performance on Test set #1 and #2, due to the integration of anatomical knowledge, ensembling, and tumor candidate classification, underscoring the potential of our approach for NF segmentation. Whereas the interactive DINs method performed well, our method achieved competitive performance on Test set #1 with no manual intervention.

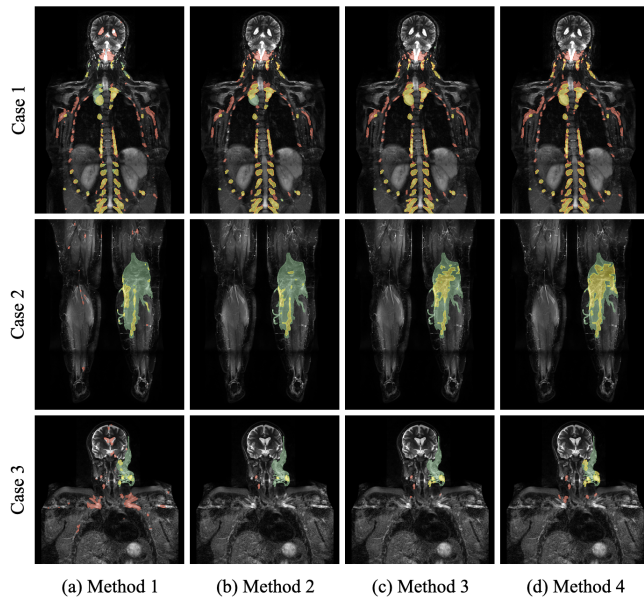


Fig. 7. Comparison of neurofibroma segmentation results showing true positives (yellow), false positives (red), and false negatives (green) across three exemplar cases (rows) and four methods (columns): (a) Method 1 (3D isotropic U-Net), (b) Method 2 (3D anisotropic U-Net), (c) Method 3 (ensemble of 3D anisotropic anatomy-informed U-Nets), (d) Method 4 (Method 3 with high-confidence tumor candidate classification). Cases: (1) 25-year-old male with 626 tumors (3715.4 cm³), (2) 55-year-old female with 4 tumors (734.7 cm³), (3) 21-year-old female with 1 tumor (470.1 cm³).

3) Limitations and Further Directions: Despite improvements, a key limitation of our method is sensitivity to domain shifts; a tumor candidate classifier trained on radiomic features from 3T MRI may not generalize well to 1.5T MRI data, emphasizing the need for feature harmonization. Performance also declines with sparse or small tumors (Test set #3), suggesting the integration of interactive segmentation for low tumor burden cases. Additionally, there is a need for standardized evaluation protocols in NF segmentation to enable consistent comparisons across studies.

B. Limitations of Existing Evaluation Protocols

As outlined in Table VI, multiple protocols and strategies exist for evaluating NF segmentation. Although recent studies adopted DSC to measure segmentation accuracy, DSC can be calculated differently depending on the study: in 2D or 3D, per tumor or over all tumors in a scan. Size thresholds for the inclusion of tumors in the evaluation also differ, with some studies using 75 cm³ as a minimum [9], [11], whereas others include tumors as small as 5 cm³ [10], [14], [15]. This lack of a unified evaluation protocol complicates direct comparisons between segmentation methods [9]–[12].

Per-scan DSC, commonly used in evaluation of DL-based methods, has limitations in the case of NF task, characterized by many small tumors spread across the body. Per-scan DSC is heavily skewed by background voxels in WB-MRI, and excluding the background increases sensitivity to small errors, resulting in high variability, especially in datasets with few tumors (e.g., Test set #3).

TABLE VI
SUMMARY OF EVALUATION PROTOCOLS USED FOR NEUROFIBROMA SEGMENTATION METHODS, INCLUDING STUDY DETAILS AND METRICS

Study	Evaluation mode	Reported Metrics
Solomon <i>et al.</i> [11], 2004	Individual tumors within ROIs in 3D	<ul style="list-style-type: none"> • Correlation between volumes • Coefficient of variation for repeatability assessment • Segmentation time
Weizman <i>et al.</i> [9], 2012	Individual / multiple tumors within ROIs in 3D	<ul style="list-style-type: none"> • Absolute volume error • Overlap error • Inter-rater variability • Segmentation time
Weizman <i>et al.</i> [14], 2013	Individual / multiple tumors within ROIs in 3D	<ul style="list-style-type: none"> • Absolute volume difference • Volume overlap error • Absolute surface distance • Intra-observer variability • Correlation between methods • Segmentation time
Pratt <i>et al.</i> [10], 2015	Individual / multiple tumors within ROIs in 3D	<ul style="list-style-type: none"> • Volume overlap error • Correlation between methods • Intra- and inter-observer variability • Segmentation time
Wu <i>et al.</i> [15], 2020	Individual tumors within ROIs in 2D	<ul style="list-style-type: none"> • Intersection over Union • Dice Similarity Coefficient • Boundary F score • Weighted Coverage • F1 score • Average Precision
Ho <i>et al.</i> [13], 2020	Individual tumors within ROIs in 3D	<ul style="list-style-type: none"> • Dice Similarity Coefficient • Volume difference • Segmentation time
Zhang <i>et al.</i> [12], 2021	All tumors in a scan in 3D	<ul style="list-style-type: none"> • Dice Similarity Coefficient • Volumetric overlap error • Absolute relative volume difference • Number of required user interactions
Wu <i>et al.</i> [16], 2022	Individual / multiple tumors within ROIs in 2D	<ul style="list-style-type: none"> • Intersection over Union • Dice Similarity Coefficient • Boundary F • Weighted Coverage

ROIs – regions of interest.

In this regard, we evaluated the correlation between per-scan DSC and tumor burden and also examined the correlation between an alternative metric, per-tumor DSC, and respective tumor volume. Our analysis showed a moderate to strong positive correlation between per-scan DSC and tumor burden across all methods (Table VII). In contrast, per-tumor DSC had a low correlation with tumor volume.

These findings suggest that while per-scan DSC reflects overall performance, it is not robust for evaluating segmentation of multiple small NFs. Thus, the evaluation protocol for NF segmentation remains an open research question.

VII. CONCLUSION

We presented a novel automated segmentation pipeline for NF in T2w WB-MRI, incorporating anatomical knowledge through a 3D anisotropic U-Net with ensembling and radiomics-based tumor candidate classification. Our method outperformed reported fully automated methods like nnU-Net and achieved performance comparable to interactive, i.e. semi-automated methods such as DINs.

The integration into the 3D Slicer platform [17] showed promise for clinical application. However, challenges for clin-

TABLE VII

PEARSON CORRELATION COEFFICIENTS BETWEEN PER-SCAN AND PER-TUMOR DICE SIMILARITY COEFFICIENT WITH PER-SCAN TUMOR BURDEN AND TUMOR VOLUME ACROSS SEGMENTATION METHODS: (1) 3D ISOTROPIC U-NET, (2) 3D ANISOTROPIC U-NET, (3) ENSEMBLE OF 3D ANISOTROPIC ANATOMY-INFORMED U-NETS, (4) METHOD 3 WITH HIGH-CONFIDENCE TUMOR CANDIDATE CLASSIFICATION

Method i	1	2	3	4
Correlation: per-scan	0.848	0.614	0.578	0.603
p -value: per-scan	< 0.01	< 0.01	< 0.01	< 0.01
Correlation: per-tumor	0.008	0.034	0.035	0.033
p -value: per-tumor	0.550	0.012	0.011	0.016

ical application remain, including handling variations in MRI field strength and low tumor burden cases. Our analysis also indicated that current evaluation metrics, like per-scan DSC, may not adequately capture the NF segmentation complexity, especially for multiple small tumors.

Future work aims to enhance robustness against domain shifts with MRI harmonization techniques, improve performance in low-burden cases, and explore integration with interactive segmentation methods for greater flexibility. We also advocate for the development of standardized evaluation frameworks to ensure consistent comparisons in NF segmentation research.

REFERENCES

- [1] M. Lammert *et al.*, "Prevalence of Neurofibromatosis 1 in German Children at Elementary School Enrollment," *Archives of Dermatology*, vol. 141, no. 1, 2005.
- [2] J. M. Friedman and P. H. Birch, "Type 1 neurofibromatosis: A descriptive analysis of the disorder in 1,728 patients," *American Journal of Medical Genetics*, vol. 70, no. 2, pp. 138–143, 1997.
- [3] U. Thakur *et al.*, "Multiparametric whole-body MRI of patients with neurofibromatosis type I: spectrum of imaging findings," *Skeletal Radiology*, pp. 1–16, 2024, <https://doi.org/10.1007/s00256-024-04765-6>.
- [4] S. R. Plotkin *et al.*, "Quantitative Assessment of Whole-Body Tumor Burden in Adult Patients with Neurofibromatosis," *PLoS ONE*, vol. 7, no. 4, p. e35711, 2012.
- [5] D. G. R. Evans, "Malignant peripheral nerve sheath tumours in neurofibromatosis 1," *Journal of Medical Genetics*, vol. 39, no. 5, pp. 311–314, 2002.
- [6] S. Ahlawat *et al.*, "Current status and recommendations for imaging in neurofibromatosis type 1, neurofibromatosis type 2, and schwannomatosis," *Skeletal Radiology*, vol. 49, no. 2, pp. 199–219, 2020.
- [7] W. P. Chan, "Magnetic resonance imaging of soft-tissue tumors of the extremities: A practical approach," *World Journal of Radiology*, vol. 5, no. 12, pp. 455–459, 2013.
- [8] M. A. Heffler *et al.*, "Tumor segmentation of whole-body magnetic resonance imaging in neurofibromatosis type 1 patients: tumor burden correlates," *Skeletal Radiology*, vol. 46, no. 1, pp. 93–99, 2017.
- [9] L. Weizman *et al.*, "Interactive segmentation of plexiform neurofibroma tissue: method and preliminary performance evaluation," *Medical & Biological Engineering & Computing*, vol. 50, no. 8, pp. 877–884, 2012.
- [10] L. Pratt *et al.*, "Tumor burden evaluation in NF1 patients with plexiform neurofibromas in daily clinical practice," *Acta Neurochirurgica*, vol. 157, no. 5, pp. 855–861, 2015.
- [11] J. Solomon *et al.*, "Automated detection and volume measurement of plexiform neurofibromas in neurofibromatosis 1 using magnetic resonance imaging," *Computerized Medical Imaging and Graphics*, vol. 28, no. 5, pp. 257–265, 2004.
- [12] J.-W. Zhang *et al.*, "DINs: Deep Interactive Networks for Neurofibroma Segmentation in Neurofibromatosis Type 1 on Whole-Body MRI," *IEEE Journal of Biomedical and Health Informatics*, vol. 26, no. 2, pp. 786–797, 2022.
- [13] C. Y. Ho *et al.*, "Image segmentation of plexiform neurofibromas from a deep neural network using multiple b-value diffusion data," *Scientific Reports*, vol. 10, no. 1, p. 17857, 2020.
- [14] L. Weizman *et al.*, "PNist: interactive volumetric measurements of plexiform neurofibromas in MRI scans," *International Journal of Computer Assisted Radiology and Surgery*, vol. 9, no. 4, pp. 683–693, 2014.
- [15] X. Wu *et al.*, "Deep Parametric Active Contour Model for Neurofibromatosis Segmentation," *Future Generation Computer Systems*, vol. 112, pp. 58–66, 2020.
- [16] —, "DH-GAC: deep hierarchical context fusion network with modified geodesic active contour for multiple neurofibromatosis segmentation," *Neural Computing and Applications*, 2022, <https://doi.org/10.1007/s00521-022-07945-4>.
- [17] A. Fedorov *et al.*, "3D Slicer as an Image Computing Platform for the Quantitative Imaging Network," *Magnetic resonance imaging*, vol. 30, no. 9, pp. 1323–1341, 2012.
- [18] H. Hüntze *et al.*, "MRSegmentator: Robust Multi-Modality Segmentation of 40 Classes in MRI and CT Sequences," 2024, arXiv:2405.06463 [cs, eess]. [Online]. Available: <http://arxiv.org/abs/2405.06463>
- [19] A. Diaz-Pinto *et al.*, "DeepEdit: Deep Editable Learning for Interactive Segmentation of 3D Medical Images," in *Data Augmentation, Labelling, and Imperfections*, H. V. Nguyen, S. X. Huang, and Y. Xue, Eds. Cham: Springer Nature Switzerland, 2022, vol. 13567, pp. 11–21, series Title: Lecture Notes in Computer Science.
- [20] K. Staser, F.-C. Yang, and D. W. Clapp, "Pathogenesis of Plexiform Neurofibroma: Tumor-Stromal/Hematopoietic Interactions in Tumor Progression," *Annual Review of Pathology: Mechanisms of Disease*, vol. 7, no. 1, pp. 469–495, 2012.
- [21] C. Palmer *et al.*, "Analysis of neurofibromatosis 1 (NF1) lesions by body segment," *American Journal of Medical Genetics Part A*, vol. 125A, no. 2, pp. 157–161, 2004.
- [22] A. Kirillov *et al.*, "Segment Anything," 2023, arXiv:2304.02643 [cs]. [Online]. Available: <http://arxiv.org/abs/2304.02643>
- [23] A. Hatamizadeh *et al.*, "UNETR: Transformers for 3D Medical Image Segmentation," 2021, arXiv:2103.10504 [cs, eess]. [Online]. Available: <http://arxiv.org/abs/2103.10504>
- [24] —, "Swin UNETR: Swin Transformers for Semantic Segmentation of Brain Tumors in MRI Images," in *Brainlesion: Glioma, Multiple Sclerosis, Stroke and Traumatic Brain Injuries*, A. Crimi and S. Bakas, Eds. Cham: Springer International Publishing, 2022, vol. 12962, pp. 272–284, series Title: Lecture Notes in Computer Science.
- [25] S. Ahlawat *et al.*, "Current whole-body MRI applications in the neurofibromatoses: NF1, NF2, and schwannomatosis," *Neurology*, vol. 87, no. 7-Supplement_1, 2016.
- [26] F. Isensee *et al.*, "nnU-Net: a self-configuring method for deep learning-based biomedical image segmentation," *Nature Methods*, vol. 18, no. 2, pp. 203–211, 2021.
- [27] J. J. Van Griethuysen *et al.*, "Computational Radiomics System to Decode the Radiographic Phenotype," *Cancer Research*, vol. 77, no. 21, pp. e104–e107, 2017.
- [28] I. Ristow *et al.*, "Evaluation of magnetic resonance imaging-based radiomics characteristics for differentiation of benign and malignant peripheral nerve sheath tumors in neurofibromatosis type 1," *Neuro-Oncology*, vol. 24, no. 10, pp. 1790–1798, 2022.
- [29] C. Y. M. N. Jansma *et al.*, "Preoperative Classification of Peripheral Nerve Sheath Tumors on MRI Using Radiomics," *Cancers*, vol. 16, no. 11, p. 2039, 2024.
- [30] E. Lavrova *et al.*, "A review of handcrafted and deep radiomics in neurological diseases: transitioning from oncology to clinical neuroimaging," 2024, arXiv:2407.13813 [cs, eess, q-bio]. [Online]. Available: <http://arxiv.org/abs/2407.13813>
- [31] L. Breiman, "Random Forests," *Machine Learning*, vol. 45, no. 1, pp. 5–32, 2001.
- [32] National Institutes of Health, "Neurofibromatosis. Conference statement. National Institutes of Health Consensus Development Conference," *Archives of Neurology*, vol. 45, no. 5, pp. 575–578, 1988.
- [33] M. J. Cardoso *et al.*, "MONAI: An open-source framework for deep learning in healthcare," Nov. 2022. [Online]. Available: <https://github.com/Project-MONAI/MONAI>